

## ATLAS: A HIGH-CADENCE ALL-SKY SURVEY SYSTEM

J. L. TONRY,<sup>1</sup> L. DENNEAU,<sup>1</sup> A. N. HEINZE,<sup>1</sup> B. STALDER,<sup>2</sup> K. W. SMITH,<sup>3</sup> S. J. SMARTT,<sup>3</sup>  
C. W. STUBBS,<sup>4</sup> H. J. WEILAND,<sup>1</sup> AND A. REST<sup>5,6</sup>

<sup>1</sup>*Institute for Astronomy, University of Hawaii, 2680 Woodlawn Drive, Honolulu, HI 96822*

<sup>2</sup>*LSST, 950 N. Cherry Ave, Tucson, AZ 85719*

<sup>3</sup>*Astrophysics Research Centre, School of Mathematics and Physics, Queen's University Belfast, Belfast, BT7 1NN, UK*

<sup>4</sup>*Department of Physics, Harvard University, Cambridge, MA 02138, USA*

<sup>5</sup>*Space Telescope Science Institute, 3700 San Martin Drive, Baltimore, MD 21218, USA*

<sup>6</sup>*Department of Physics and Astronomy, Johns Hopkins University, Baltimore, MD 21218, USA*

### ABSTRACT

Technology has advanced to the point that it is possible to image the entire sky every night and process the data in real time. The sky is hardly static: many interesting phenomena occur, including variable stationary objects such as stars or QSOs, transient stationary objects such as supernovae or M dwarf flares, and moving objects such as asteroids and the stars themselves. Funded by NASA, we have designed and built a sky survey system for the purpose of finding dangerous near-Earth asteroids (NEAs). This system, the “Asteroid Terrestrial-impact Last Alert System” (ATLAS), has been optimized to produce the best survey capability per unit cost, and therefore is an efficient and competitive system for finding potentially hazardous asteroids (PHAs) but also for tracking variables and finding transients. While carrying out its NASA mission, ATLAS now discovers more bright ( $m < 19$ ) supernovae candidates than any ground based survey, frequently detecting very young explosions due to its 2 day cadence. ATLAS discovered the afterglow of a gamma-ray burst independent of the high energy trigger and has released a variable star catalogue of  $5 \times 10^6$  sources. This is the first of a series of articles describing ATLAS, devoted to the design and performance of the ATLAS system. Subsequent articles will describe in more detail the software, the survey strategy, ATLAS-derived NEA population statistics, transient detections, and the first data release of variable stars and transient lightcurves.

*Keywords:* surveys; minor planets, asteroids: general; stars: variables: general; supernovae: general

[tonry@hawaii.edu](mailto:tonry@hawaii.edu)

[denneau@hawaii.edu](mailto:denneau@hawaii.edu)

[aheinze@hawaii.edu](mailto:aheinze@hawaii.edu)

[bstalder@lsst.org](mailto:bstalder@lsst.org)

[k.w.smith@qub.ac.uk](mailto:k.w.smith@qub.ac.uk)

[s.smartt@qub.ac.uk](mailto:s.smartt@qub.ac.uk)

[stubbs@g.harvard.edu](mailto:stubbs@g.harvard.edu)

[hweiland@hawaii.edu](mailto:hweiland@hawaii.edu)

[arest@stsci.edu](mailto:arest@stsci.edu)

## 1. INTRODUCTION

The remarkable progress of silicon technology in recent decades has made it possible to examine the entire sky for moving, variable, or transient objects every night to a meaningful depth. Optimizing survey performance is a complex task, however. Resources need to be divided between the cost of a facility to protect the system from the elements; a telescope, a mount, and a detector to collect the light; and computers, operations, and software to run the survey and process the results. Any of these features can limit performance.

Combining the detector technology advances with venerable Schmidt telescopes or newly designed wide-field facilities has rapidly changed the astronomical survey landscape in the last few years. The ambitious Pan-STARRS1 survey (PS1; [Chambers et al. 2016](#)) has mapped  $3\pi$  steradians of the sky (30,000 square degrees) in 6 wavebands and is having a major impact — not only in transients and moving objects ([Hsieh et al. 2012](#); [Rest et al. 2014](#)) but from low mass stars ([Liu et al. 2013](#)), through Milky Way stellar populations ([Laevens et al. 2015](#)) to the highest redshift quasars ([Bañados et al. 2014](#)). The Palomar Transient Factory (PTF; [Law et al. 2009](#)) reinvigorated the scientific capability of the Palomar Schmidt telescope producing a wide range of discoveries of novel objects (e.g. [Quimby et al. 2011](#); [Gal-Yam et al. 2011](#); [Cenko et al. 2013](#)). PTF has been upgraded to the Zwicky Transient Facility (ZTF) ([Bellm 2014](#)) with a much larger field of view. The QUEST camera was installed on the Schmidt telescope at La Silla to run the La Silla QUEST survey, (LSQ; [Baltay et al. 2013](#)) which combined with the the Public ESO Spectroscopic Survey of Transient Objects (PESSTO [Smartt et al. 2015](#)) for spectroscopic follow-up, again producing a range of discoveries (e.g. [Nicholl et al. 2014, 2015](#)). The Catalina Real Time Survey (CRTS; [Drake et al. 2009](#)) is a very successful time-domain survey which has influenced survey science from the solar system through supernovae and AGN variability. The SkyMapper survey ([Keller et al. 2007](#)) is now producing its first public data products, completing the multi-color coverage of the whole sky ([Wolf et al. 2018](#)). Other surveys on large aperture telescopes such as the Dark Energy Survey ([Dark Energy Survey Collaboration et al. 2016](#)) and HyperSuprimeCam ([Moriya et al. 2018](#)) are now playing a major role with exceptional depth and photometric performance over smaller sky areas. At the other end, novel use and fast processing of data from small 14cm lens systems by the All-Sky Automated Survey for SuperNovae (ASSASN; [Holoien et al. 2017](#)) have been impressively productive, providing some rare and surprising finds ([Dong et al. 2016](#)). From the tens of centimeters to 10m sized apertures, survey astronomy truly has changed in the last few years; a revolution that has made it into orbit with ESA’s Gaia facility using its scanning capability to produce transient alerts ([Hodgkin et al. 2013](#); [Walton et al. 2015](#); [Gaia Collaboration et al. 2016](#)).

ATLAS was proposed as a replicable system that NASA could use to find dangerous asteroids, and optimization for the NASA mission opens synergistic opportunities for many other types of science ([Tonry 2011](#)). Predicting asteroid collisions with Earth places constraints on system capability, for example, warning of at least one day for a  $\sim 1$  Mton explosion requires all-sky monitoring at a sensitivity of  $m > 19$ . Funded in 2013, ATLAS achieved first light in June 2015 and now consists of two independent units, one on Haleakala (HKO), and one on Mauna Loa (MLO) in the Hawai’ian islands.

A number of papers have been written about sky survey design and optimization including [Tonry \(2011\)](#), [Terebizh \(2011, 2016\)](#), and [Bellm \(2016\)](#). [Tonry \(2011\)](#) summarized survey performance in terms of a “survey speed” that expresses the rate at which objects can be observed to a limiting

magnitude  $m$  with signal to noise ratio SNR. In the background limited, random distribution on sky, Poisson regime this becomes

$$SS = \frac{A \Omega_0 \epsilon \delta}{\omega} 10^{+0.4(\mu+m_0-2m_s)} = \frac{\text{SNR}^2 \Omega}{t_{cad}} 10^{+0.8(m-m_s)} \quad (1)$$

where  $A$  [m<sup>2</sup>] is the collecting area,  $\Omega_0$  [deg<sup>2</sup>] is the solid angle covered by the detector,  $\epsilon$  is the efficiency for light to be detected (relative to a fiducial  $m_0 = 25.10$  that provides 1 photon per second per m<sup>2</sup> per 0.2 in natural log of bandpass),  $\delta$  is the duty cycle over cadence time  $t_{cad}$  [sec] that the shutter is open,  $\omega$  [arcsec<sup>2</sup>] is the point spread function (PSF) noise footprint solid angle (essentially  $3.5d^2$  where  $d$  is the PSF full width half maximum, FWHM),  $\mu$  is the sky brightness [mag/arcsec<sup>2</sup>],  $\Omega$  [deg<sup>2</sup>] is net solid angle surveyed during  $t_{cad}$ , and  $m_s$  is a desired survey depth. In effect, the left hand side of equation 1 describes a survey in design, how well it ought to perform, the right hand side describes a survey in operation, how well it actually performs.

Because this equation describes an extensible quantity, it is possible to examine tradeoffs, such as doubling the collecting area or building two identical systems in order to double the rate at which objects can be found. Less obvious trades that double the rate include halving the PSF footprint solid angle  $\omega$ , looking for objects that are 0.4 mag brighter, or lowering the SNR requirement. Since the bottom line for many surveys is how many objects can be surveyed per unit time and the bottom line for any project is how productive it is per unit resource, the metric by which a survey project should be judged is survey speed per unit cost.

Tonry (2011) showed that an array of 0.25 m astrographs could inexpensively observe all sky each night to  $m \sim 19$ . The actual implementation of the funded ATLAS program employs 0.5 m Schmidt telescopes rather than an array of smaller telescopes, in order to optimize with respect to telescope and detector cost — advent of 10k CCDs brought the marginal cost of telescope improvement below that of detector improvement relative to the original design.

The relevant design numbers for one ATLAS unit are  $A = 0.14$  m<sup>2</sup> (including vignetting),  $\Omega_0 = 29$  deg<sup>2</sup>,  $\epsilon = 1.25$  for transmission through atmosphere, optics, detector QE, and  $o$  filter bandpass width,  $\delta = 0.75$ ,  $\omega = 52$  arcsec<sup>2</sup> for 2 pixel FWHM PSF,  $\mu = 20.7$  mag/arcsec<sup>2</sup>, and  $m_s = 20$ , for a predicted speed of  $SS = 15$  deg<sup>2</sup>/sec. What an ATLAS unit can actually achieve in a 30 sec exposure and 40 sec cadence in  $c$  or  $o$  band is  $m_{5\sigma} \sim 19.7$ , corresponding to a “best condition” survey speed of  $SS = 10$  deg<sup>2</sup>/sec, less than Eq. 1 because Eq. 1 does not include the terms for read noise or dark current. While survey speed might be made more useful by using median limiting magnitude and including a term for weather losses (diminishing the ATLAS  $SS$  to 3 deg<sup>2</sup>/sec), evaluating whether a system is performing to its design potential requires best case numbers. An ATLAS unit costs \$1M to replicate (including everything from enclosure to software), so this ratio of survey speed to cost sets the value metric for ATLAS.

As far as we can tell from published or estimated numbers, the best condition  $SS$  for other surveys at  $m_s = 20$  includes  $\sim 0.4$  deg<sup>2</sup>/sec for a single ASASSN unit ( $g$  filter),  $\sim 7$  and  $\sim 50$  deg<sup>2</sup>/sec for Catalina’s Schmidt and 60” telescopes (unfiltered),  $\sim 100$  deg<sup>2</sup>/sec for ZTF ( $r$  filter),  $\sim 700$  deg<sup>2</sup>/sec for each Pan-STARRS telescope ( $w$  filter), and  $\sim 25,000$  deg<sup>2</sup>/sec for LSST ( $r$  filter). Use of filters causes a loss of  $SS$  but is offset by the scientific value of spectral information, and is a choice driven by the goals of a survey system. Of course different surveys are designed for different  $m_s$ , so ASASSN

cannot do LSST's job nor LSST ASASSN's job, but we encourage the use of this methodology for design, optimization, and comparison of new survey capability.

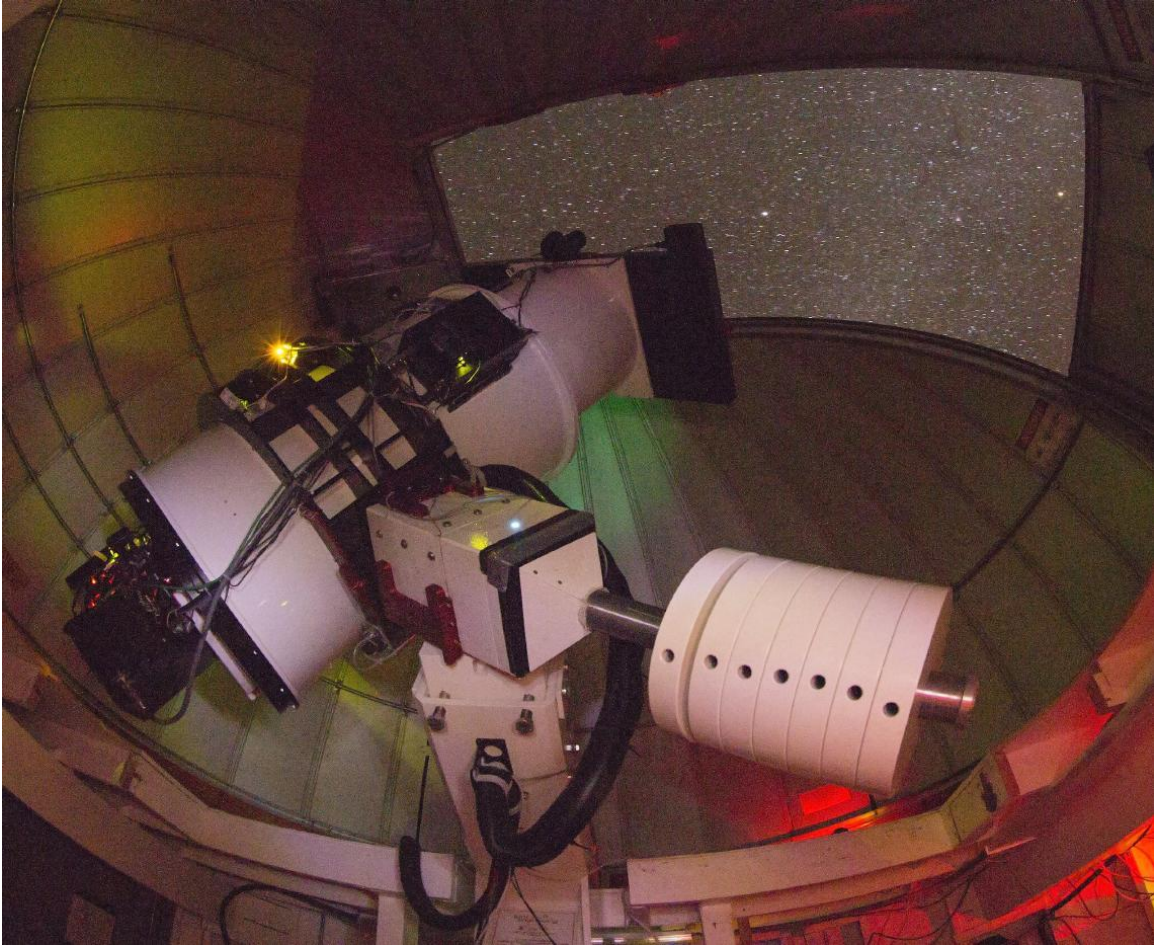


**Figure 1.** The ATLAS unit on Haleakala from inside the dome.

Autonomous operation is another requirement for a cost efficient survey, as well as enabling the low latency processing and discovery essential for impending impacts. For the NASA mission, ATLAS has built a system that consists of summit operations, reduction pipeline, and a science client that processes the output for moving objects. The summit operations automatically close, open, and observe when possible, following an automatic schedule. The reduction pipeline calibrates the images, subtracts from them a static sky image, and produces a table of detections of sources that have changed from the static sky. The moving object science client waits until multiple observations arrive for a given area on the sky and then links detections into plausible asteroid tracklets. Candidate unknown asteroids are screened by a human for accuracy and are then posted to the Minor Planet Center, who coordinates followup of unknown near-Earth asteroids.

Other science clients also tap the results from the sky subtracted images. Using computer resources at Queen's University Belfast (QUB), we search the same detection tables for stationary transients. These stationary transients are spatially matched against star, galaxy, active galactic nuclei, and QSO catalogues. The variable objects are filtered out leaving supernova candidates which are auto-

matically reported publicly to the International Astronomical Union (IAU) Transient Name Server (TNS, Smith et al. *in prep.*). We also mirror all the ATLAS raw data at QUB as a safe, off-site backup. ATLAS is designed and operated to be optimal for asteroid discovery, but the sky survey synergistically contributes significant results in many other science areas.

- Among regionally dangerous ( $> 30\text{m}$ ) asteroids detected during very close approaches ( $< 0.01\text{AU}$ ) to the Earth, ATLAS detects as many or more than any other asteroid survey, demonstrating its successful optimization as a ‘Last Alert’ system for potential impactors.
- Up to the end of 2017, ATLAS reported 1175 candidate supernovae to the IAU Transient Name Server <sup>1</sup>. Notable discoveries include detection of the shock break-out signature of SN2016gkg (Arcavi et al. 2017a) and the discovery of the unusual interacting type Ic supernova SN2017dio (Kuncarayakti et al. 2017).
- Between 1 Jan 2016 and 18 Mar 2018, ATLAS has discovered the most spectroscopically classified transient objects (311, compared to ASASSN’s 307), as reported in the TNS. This is enabling a host of ongoing science projects. For example, through an alliance with the Public ESO Spectroscopic Survey for Transient Objects (PESSTO; Smartt et al. 2015), ATLAS provides young supernovae for the Foundation Supernova Survey (Foley et al. 2018), working to create a definitive low redshift type Ia supernova sample to anchor cosmological analyses.
- The large nightly ATLAS sky footprint has allowed searches for counterparts of gravitational wave sources from the LIGO - Virgo collaboration. During the first two observing runs ATLAS was a signatory to the agreement to share triggers. We searched for possible bright counterparts to binary black hole (BBH) mergers and discovered the afterglow of a gamma ray burst (GRB) before the high energy source was localized on the sky (Stalder et al. 2017). This object, ATLAS17aeu, was discovered within the sky map of GW170104 (Abbott et al. 2017a), but is likely an unrelated GRB exploding 24hrs after the gravitational wave trigger. This is only the third GRB afterglow detected independently of a high energy trigger (the others discovered by Cenko et al. 2013, 2015).
- A merging neutron star system produced the source GW170817 (Abbott et al. 2017b,c) and was accompanied by the discovery of an optical and near-infrared bright kilonova. It was discovered in NGC4993 at a distance of only 40 Mpc by several telescopes as soon as night fell in Chile (Arcavi et al. 2017b; Coulter et al. 2017; Lipunov et al. 2017; Soares-Santos et al. 2017; Tanvir et al. 2017; Valenti et al. 2017). ATLAS had been continually observing NGC4993 until 16 days before GW170817, and we showed it was not a variable source over the previous 601 days (Smartt et al. 2017, see also Valenti et al. 2017). ATLAS will provide meaningful limits on the rate of kilonovae (irrespective of GW triggers) within 60 Mpc (Scolnic et al. 2018, and Coughlin et al. *in prep.*).
- During its first two years ATLAS observed 140 million stars hundreds of times and has detected variability (pulsation, rotation, occultations, outbursts) in 5 million objects (Heinze et al. *in prep.*). We will be releasing these lightcurves through the Mikulski Archive for Space Telescopes

<sup>1</sup> <https://wis-tns.weizmann.ac.il>

(MAST). The ensuing 6 months has doubled the number of detections and increased the number of stars to 240 million, and there will be periodic data releases and updates.

- Asteroid characterization: color, rotation, volatile emission, and collisions are all measurable in the ATLAS lightcurves.
- ATLAS regularly detects satellites in geosynchronous orbit and beyond, and our multiple observations allow us to determine accurate 3D positions and velocities.

The NEA optimised survey strategy employed by the first two ATLAS units is equally good for transients and variables. We view the ATLAS unit as an inexpensive, reproducible system that could be deployed at sites judiciously separated in latitude and longitude to give 24hr, all sky coverage to  $m \sim 20$  with a 1-day multi-exposure cadence. This paper is the first in a series describing the ATLAS hardware and software systems. It gives a broad overview of all the components that make the survey functional, more specialised papers are in preparation giving details of the subsystems.

## 2. ENCLOSURE

We considered a number of possible enclosures for ATLAS including traditional Ash domes with an over-the-top shutter, clamshell designs such as Astrohaven, and enclosures with roll-off roofs. We even designed “ATLAS-in-a-can”, an ATLAS unit in a commodity truck with a fold-off roof and a hole in the floor so the mount could be lowered onto a solid pedestal. As far as we know “ATLAS-in-a-can” would perform well, and with a very compliant shipping truss to hold the ATLAS telescope and mount within the truck as well as the truck’s suspension, transportation would be simple and safe.

Concerns over wind buffeting, water leakage in severe storms, ambient light and overall reliability led us to choose Ash domes as the ATLAS enclosure. Because we must operate autonomously, reliability is an extremely important consideration. We do create unusual stress on the Ash dome by rotating every  $\sim 40$  sec, which leads to bolts loosening, so threadlocking adhesive on most fasteners is a required upgrade from the nominal Ash construction.

The dome is a standard 16.5 foot diameter half-sphere over an 8 foot tall cylinder. The pier is offset south from the center by 14 inches and is 41 inches tall and 30 inches diameter. Steel rebar is epoxied into the slab to provide stiffening and support for the concrete pier. We modified the Ash dome by adding I-beam mount points for a 500 pound rated chain hoist and by putting a Canarm 20-inch exhaust fan in the wall which has motorized louvers that close when not in operation. During daylight hours in good weather we open the dome slit by 6 inches for air intake and run the exhaust fan continuously. This keeps the interior of the dome close to ambient temperature. Without the fan, the sun beating down on the aluminum greatly increases the air temperature inside the dome, resulting in bad seeing during the early part of the night and unnecessary thermal stress on the equipment.

The Ash domes use a servo loop controlled stepper motor, and therefore have precise acceleration and movement. The absolute zero position is set by a switch that is engaged at a particular position and the position thereafter is known by counts. The domes use slip rings to get power to the shutter motor, so have no limitations on rotation. We have some concerns that our  $\sim 900$  dome moves each night may be causing inordinate wear, but so far our monthly maintenance has revealed no more than bolts vibrating loose and needing to be retightened. The dome angular velocity is about 3.75 deg/sec

and about 2 sec is spent in acceleration, so the dome can move  $\sim 25^\circ$  during the  $\sim 9$  sec of CCD readout and shutter overhead.

In addition to the normal electrical wiring required, we built a “mezzanine loft” and stairs that permit easy access to the telescope. The following equipment supports the operations of mount, telescope, and camera:

- Switch and fiber connections to our “computer room”.
- Various “low power” industrial computers, one running Windows to interface to the DFM telescope (see Section 4), another running Linux with a dedicated ethernet to the camera controller.
- Various Raspberry-pi computers to provide IP network interfacing with individual devices (dome, Canon cameras, etc)
- ThermoFisher Accel 500 water chiller for CCD cooling.
- Puregas CDA-10 dehumidifier for mitigating moisture condensation on the camera window.
- A pair of webcams, a microphone, and an Ipod Touch to monitor the inside of the dome and communicate with personnel working at the summit.
- Keyboard and monitor for on-site manual control and system monitoring.
- A “fail safe” Raspberry-pi that uses a Hydreon rain sensor and monitors the electrical power to the dome. If the power fails or the Hydreon reports rain or mist this computer closes the dome immediately.
- Various uninterruptible power supplies (UPS) to provide temporary power while the observatory safely shuts down automatically.
- A fisheye camera and meteorology box located nearby provides environmental telemetry (see Section 7).

### 3. MOUNT

We considered an equatorial mount to be essential, since an az-alt mount and image rotator adds significant risk of technical failure. Furthermore, the degraded performance near the zenith for an az-alt telescope causes problems for an all-sky survey.

The ATLAS mount is a German equatorial mount (GEM) built by APM Telescopes of Saarbruecken Germany. We considered a fork mount, but for a telescope of this size a GEM is simpler, less expensive, and the advantage of cable routing for a fork mount is not a significant factor at this scale. The APM mount has 7 large counterweights of about 35 kg apiece to counterbalance the mass of the telescope.

This mount is very fast. The slew velocity is 15 deg/sec, and for moves smaller than 45 deg the time to slew and resume tracking is  $6.5 \pm 0.8$  sec, comfortably less than the CCD readout time. A meridian flip requires a rotation of  $\sim 180^\circ$  in both axes and typically takes 25 sec. Our scheduling software is mindful of the cost of a meridian flip and minimizes them.

There are small issues with servo loop stability that occasionally cause some image elongation. Re-tuning the servo parameters cures this, but we do not fully understand why it returns. Winds higher

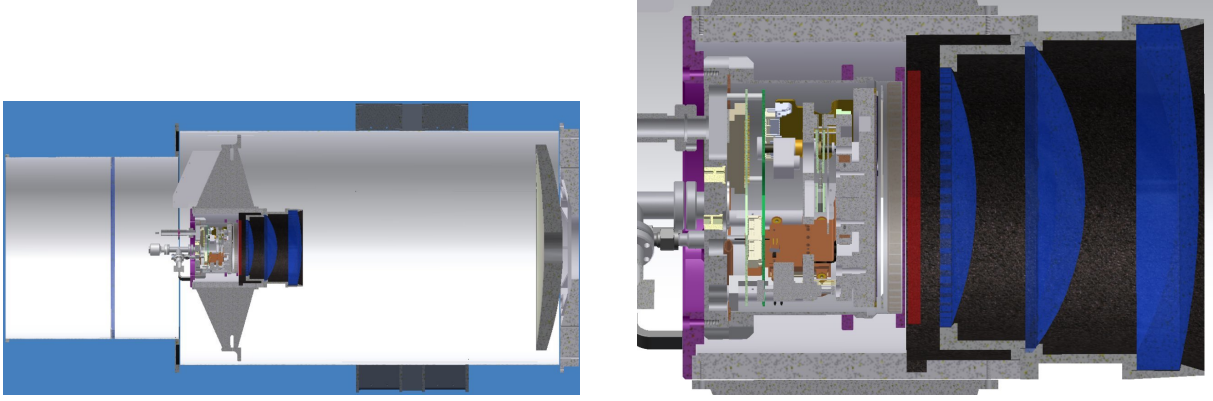


**Figure 2.** Left: Light enters the Schmidt corrector of the DFM telescope (thin blue section on the left), passes the prime focus supported by a spider assembly, reflects off of the primary mirror on the right, returns through field correctors (three blue lenses), a filter (magenta), and a cryostat window (gray) before arriving at the detector. The overall length from shutter to back of mirror cell is 1.9 m, the focus unit adding another 0.4 m, and the diameter of the mirror cell is 0.8 m. Right: A detail of the field lens and camera assembly illustrates the close spacing of the third field lens, filter, cryostat window, and CCD. The distance from Schmidt corrector to back of cryostat is 0.26 m, from there to the first field lens is 0.33 m, and the diameter of the field corrector and camera housing is 0.25 m.

than  $40 \text{ km h}^{-1}$  can buffet the large shutter at the top of the telescope depending on dome position, elongating the images. (The wind speed is measured by a Boltwood sensor; ATLAS is allowed to open for speeds below 30 kph and is required to close for speeds above 60 kph.) The APM mount can track in both axes, and we have an elaborate and accurate mount model. Since our exposures are short, we do not need to have perfect polar alignment.

#### 4. TELESCOPE

Our telescopes were designed and built by DFM Engineering of Longmont, Colorado. They are a variant of a “Wright Schmidt”, the optical train is a 0.5 m Schmidt corrector, an 0.65 m spherical primary mirror, a three element field corrector, a filter, the cryostat window, and the detector. These are illustrated in Figure 2.

The overall focal length is 1.0 m, for a system  $f$ -ratio of  $f/2.0$ . The optics perform well over a field diameter of about  $7.5^\circ$ , and are designed to have modest chromatic aberration over the broad cyan bandpass ( $c$ , covering 420-650 nm) used by ATLAS, but images are distinctly sharper in our redder survey bandpasses, called orange ( $o$ , 560-820 nm). The oversized primary mirror minimizes vignetting. The field corrector assembly and camera housing shown in Figure 2 has a maximum diameter of 250mm which determines the amount of central pupil obscuration.

The first telescope was installed on Haleakala in Jun 2015 and the second in Feb 2017 on Mauna Loa. The figure on the Schmidt correctors was not perfect however, and the delivered image quality on the focal plane for the first telescope was about 3.8 pixels FWHM ( $7''$ ) when initially installed. Efforts to improve the second corrector at DFM were not successful so we initiated a contract with Coherent Technologies (Tinsley) for a pair of corrector lenses. These were installed in May 2017 on both ATLAS units and the telescopes were collimated. The optics on Haleakala do an excellent job, producing images slightly better than 2.0 pixels ( $3.5''$ ), but there is some residual astigmatism in the



corrector on Mauna Loa, so the best images are about 2.8 pixels ( $5''$ ). The astigmatism rotates with the Schmidt corrector, but was not apparent in the Tinsley test results so we are currently puzzled about its origin.

Collimation of the telescope is accomplished by adjusting push-pull screws attached to the four ends of the spider assembly. We have written ray tracing software that calculates out-of-focus donuts as a function of screw turns, so collimation proceeds by taking an out-of-focus image, assembling a mosaic of donuts across the field of view, judging from ray traces how many screw turns are required to correct the donuts, and iterating. We believe it prudent to keep human judgement in this collimation loop. Once collimated the telescopes seem to hold their adjustment very well.

The focus is performed using an absolute encoder that seems very accurate, and the telescope has an athermal design so there is extremely little focus shift as a function of temperature. The final adjustment is the tip-tilt of the detector with respect to the focal surface, and this is adjusted using the motors within the cryostat. In-focus image elongation is a sensitive diagnostic of detector tilt.

DFM also designed and provided a full aperture shutter and a filter changer. The shutter uses bi-parting blades that are carefully balanced to exert no force or torque on the telescope. At this time the shutter on Haleakala has operated nearly a million times and shows no sign of wear or degradation. The DFM filter changer comprises a cassette that holds 8 filters in frames and lifts them to an insertion mechanism that advances them into a slot between the last field corrector lens and the camera.

ATLAS filters are 125mm square and 9mm thick. We use broad band filters for our normal asteroid search, a “cyan” ( $c$ ) band from 420–650 nm, an “orange” ( $o$ ) band from 560–820 nm, and a “tomato” ( $t$ ) band from 560–975 nm intended to be differentially sensitive to the silicate band of stony asteroids relative to  $o$  band. Haleakala normally switches between  $c$  and  $o$  during survey operations in a lunation, whereas Mauna Loa stays in  $o$  or  $t$ . Table 1 provides details of our primary filters as best we currently know them.

We also have a set of filters in standard bandpasses, including one set of Johnson/Cousins filters  $B$ ,  $V$ ,  $R_c$ ,  $I_c$ , and one set of  $g$ ,  $r$ ,  $i$ ,  $z$  which are similar to SDSS and Pan-STARRS1 (Fukugita et al. 1996; Tonry et al. 2012). ATLAS also has Skymapper-like ultra-violet filters  $u$  and  $v$  (Bessell et al. 2011) and two narrow band filters centered to trace  $H\alpha$ , and [O III]. Discussions with the Skymapper team led us to adjust the center and widths of  $u$ ,  $v$ , and  $g$  to ensure better delineation than those of Bessell et al. (2011). The  $o$ ,  $c$ , Johnson, and  $H\alpha$  filters were provided by Materion (Barr), and the rest by Asahi. Details found in Table 1 and Table 2 are calculated from manufacturer’s curves for the filters, AR coatings, 1.2 airmasses of atmosphere, 0.92 reflectivity of overcoated aluminum, and the measured detector QE. The bandpasses have been adjusted for the ATLAS  $f/2$  beam using an effective index of  $n = 2$ , but no in-situ measurements have been made. Note that the  $u$ ,  $v$ , and  $z$  filters have low transmission because the field corrector AR coatings are very reflective outside of 380–850 nm. Should more ATLAS units be built we intend to open up the IR and UV transmission of the optics. Table 2 summarizes the parameters of all the ATLAS bandpasses.

Approximate conversions between ATLAS primary filters and Pan-STARRS  $g$ ,  $r$ , and  $i$  filters for stellar spectral energy distributions are given by Equation 2.

**Table 1.** ATLAS *c* and *o* Bandpasses

$\lambda$	$T_c$	$\lambda$	$T_c$	$\lambda$	$T_c$	$\lambda$	$T_o$	$\lambda$	$T_o$	$\lambda$	$T_o$
400	0.000	495	0.670	590	0.707	550	0.000	645	0.727	740	0.708
405	0.000	500	0.678	595	0.709	555	0.001	650	0.727	745	0.700
410	0.000	505	0.678	600	0.703	560	0.111	655	0.732	750	0.692
415	0.007	510	0.688	605	0.708	565	0.642	660	0.735	755	0.682
420	0.137	515	0.687	610	0.709	570	0.713	665	0.736	760	0.490
425	0.509	520	0.699	615	0.709	575	0.707	670	0.737	765	0.491
430	0.567	525	0.693	620	0.702	580	0.713	675	0.742	770	0.644
435	0.564	530	0.689	625	0.697	585	0.717	680	0.747	775	0.644
440	0.581	535	0.696	630	0.691	590	0.715	685	0.719	780	0.631
445	0.589	540	0.703	635	0.716	595	0.717	690	0.681	785	0.625
450	0.594	545	0.708	640	0.717	600	0.714	695	0.731	790	0.611
455	0.599	550	0.715	645	0.699	605	0.715	700	0.737	795	0.600
460	0.602	555	0.708	650	0.558	610	0.717	705	0.737	800	0.587
465	0.603	560	0.710	655	0.042	615	0.713	710	0.735	805	0.570
470	0.612	565	0.707	660	0.000	620	0.718	715	0.731	810	0.562
475	0.627	570	0.704	665	0.000	625	0.723	720	0.705	815	0.531
480	0.647	575	0.697	670	0.000	630	0.718	725	0.703	820	0.365
485	0.657	580	0.710	675	0.000	635	0.726	730	0.702	825	0.021
490	0.663	585	0.713	680	0.000	640	0.721	735	0.710	830	0.000

NOTE—The first six columns give wavelength [nm] and transmission of the ATLAS system in *c* band, the last six columns in *o* band (*o*1). The transmission includes 1.2 airmasses of atmosphere, mirror reflection and AR coatings, filter transmission calculated for an *f*/2 beam, and detector QE.

$$\begin{aligned}
c &\sim 0.49g + 0.51r & o &\sim 0.55r + 0.45i \\
g &\sim 1.67c - 0.67o & r &\sim 0.35c + 0.65o & i &\sim -0.39c + 1.39o \\
(c - o) &\sim 0.73 & (g - r) &\sim 0.47 & (g - i) &
\end{aligned} \tag{2}$$

## 5. CAMERA

The ATLAS camera was required to satisfy a number of requirements that could not be met by any commercial product, therefore we designed and built it in house. These requirements we imposed included:

- Fill as much of the 130 mm diameter optical field of view as possible, but sample the expected PSF of  $7\ \mu\text{m}$  RMS with pixels no larger than  $10\ \mu\text{m}$ .

**Table 2.** ATLAS Bandpass Parameters

Filter	$\langle T \rangle$	$\lambda_{eff}$	$d \ln \nu$	$\lambda_B$	$\lambda_R$	Filter	$\langle T \rangle$	$\lambda_{eff}$	$d \ln \nu$	$\lambda_B$	$\lambda_R$
<i>c</i>	0.669	533	0.290	423	651	<i>u</i>	0.032	353	0.002	344	362
<i>o(1)</i>	0.684	679	0.261	563	818	<i>v</i>	0.343	394	0.027	379	407
<i>o(2)</i>	0.680	678	0.262	561	819	<i>g</i>	0.638	484	0.175	420	549
<i>t</i>	0.641	710	0.320	558	876	<i>r</i>	0.713	619	0.166	552	691
<i>B</i>	0.545	445	0.125	394	494	<i>i</i>	0.639	751	0.112	692	818
<i>V</i>	0.621	548	0.095	509	589	<i>z</i>	0.333	892	0.054	826	940
<i>R<sub>c</sub></i>	0.665	652	0.162	577	732	<i>H<math>\alpha</math></i>	0.592	656	0.009	652	660
<i>I<sub>c</sub></i>	0.554	794	0.107	728	876	[O III]	0.592	505	0.014	500	509

NOTE—The columns are the filter, mean transmission of the system including 1.2 airmasses of atmosphere over the blue and red limits, filter “pivot” wavelength [nm] described by [Bessell & Murphy \(2012\)](#) ( $\int \lambda T(\nu) d \ln \nu / \langle T \rangle$ ), bandpass width in log wavelength times transmission (canonical 0.2 times  $\epsilon$  in Equation 1), and bandpass blue and red wavelengths [nm] obtained from a least-squares fit of a square bandpass. *o(1)* is installed on Haleakala and *o(2)* on Mauna Loa.

- Read out in less than 10 sec so that the duty cycle for a 30 sec exposure is no worse than 0.75, with a read noise of no more than  $10 e^-$ .
- Camera diameter can be no larger than 200 mm, length no longer than 200 mm, mass no more than 7 kg.
- The cryostat window is no more than 10 mm thick and distance to detector surface may be as little as 6 mm.
- The detector must be colder than  $-50^\circ \text{C}$  for dark current to be negligible compared to the sky background.
- There must be a means to remotely tip and tilt the detector to align with the f/2 focal surface.
- All connections to the camera must pass along a 3/4-inch channel on a spider vane, and the detector controller may be a distant as 0.5 m.
- The cryostat must maintain a vacuum of 1 mtorr or less for at least a year (preferably much longer) because of the difficulty in extracting the camera from the center of the telescope.

After a competitive procurement we selected STA (Semiconductor Technology Associates of San Clemente California) as the vendor for the CCDs, and chose their STA-1600 as the ATLAS detector. This is a monolithic CCD with  $10560 \times 10560$   $9 \mu\text{m}$  pixels, thinned, passivated, and AR coated by the Imaging Technology Laboratories of the University of Arizona. STA also provided the controllers and cables. We collaborated closely with STA, both on the mechanical and electrical interfaces of fitting the CCD inside the cryostat as well as tasking STA to build a custom board for ATLAS auxiliary functions such as temperature and pressure monitoring, thermoelectric cooling, and piezoelectric motor operation.

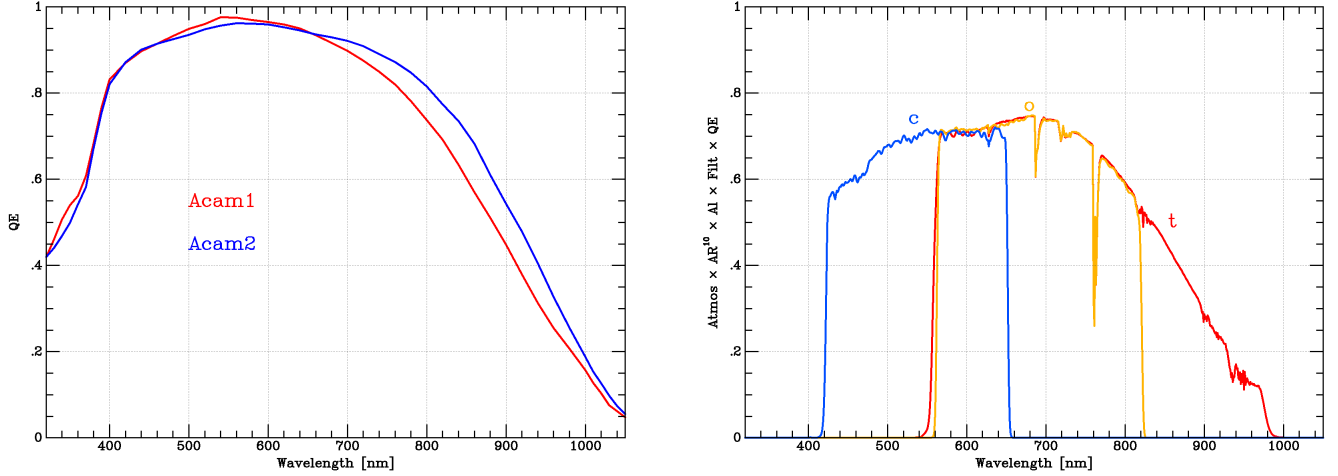


**Figure 3.** Left: The quantum efficiency measured at  $-50\text{ }^{\circ}\text{C}$  relative to a Hamamatsu photodiode with NIST-traceable calibration for our two CCDs. Right: The calculated total throughput from multiplying the traces of our primary *c* (blue), *o* (orange), and *t* (red) filters (converted to  $f/2$ ), 1.2 airmasses of extinction, AR coatings, and a factor of 0.92 for the enhanced coating on the mirror.

The cryostat consists of a 6.5-inch diameter “bell jar” that has a 3/8-inch fused silica window brazed on one end, and a standard CF-8 flange on the other end which is the solid base plate on which the internals are mounted. Outside the baseplate are a metal seal vacuum valve, an MKS micro-Pirani vacuum gauge, a Modion ion pump, a warm zeolite getter, and connectors for cooling water. Inside the cryostat are a pair of water-fed heat exchangers, a pair of two stage thermoelectric coolers (TEC), and a pair of pyrolytic graphite cold straps to a cold plate that carries the CCD. The heat exchangers have bistable thermal switches to disconnect TEC power at  $+50\text{ }^{\circ}\text{C}$  if water flow is interrupted. The cold plate is mounted on top of a flexure and is pulled down by a set of springs and pushed up by a trio of “picomotors”, vacuum rated units that use piezoelectric slabs to turn a fine pitch screw with nanometer precision. They have an enormous travel, 12 mm in our case, and are electrically inert when not in use. The position of the cold plate is monitored using linear Hall sensors that measure the radial field near the center line of a cylindrical magnet. Although we close the position loop by observing stars, we calibrate these Hall sensors in the lab using a microscope to observe the cold detector through the window, and we achieve absolute accuracies of about  $1\text{ }\mu\text{m}$ .

A pair of printed circuit boards from STA are mounted within the cryostat and are cooled by the heat exchangers. These buffer drive signals to the CCD and convert the CCD output to true differential signals that pass along the cable to the controller. This provides us with excellent noise immunity and we see no interference of any sort, even when the ion pump or picomotors are active.

The CCDs are set to a gain of about  $2\text{ }e^{-}/\text{ADU}$ , and they have a full well in excess of  $80,000\text{ }e^{-}$ . We read out at 1 MHz through 16 amplifiers so the total read time is about 9 sec. With our normal 30 sec exposure this gives a shutter-open duty cycle of about 75%. The read noise is about  $11\text{ }e^{-}$  and in a 30 second exposure the typical moonless sky background is about  $300\text{ }e^{-}$  in *c* band and  $350\text{ }e^{-}$  in *o* band, so the read noise degrades our SNR by about 16-18%. The quantum efficiency and total throughput through our two primary filters are illustrated in Figure 3.

The dark current in our STA1600 CCDs has quite a bit of pattern to it, particularly between 8 horizontal bands. The average is about  $0.8\text{ }e^{-}/\text{pix}/\text{sec}$  at a CCD temperature of  $-50\text{ }^{\circ}\text{C}$ , rising a

factor of 2 every 5 K. The thermoelectric coolers keep the CCDs at a temperature of about  $-53\text{ }^\circ\text{C}$ , so dark current is not a significant contributor to noise in our wide 250 nm *c* and *o* filters, but is a concern for our 10 nm wide narrow band filters or our UV filters. The water to the heat exchangers in the cryostat is cooled to  $+6\text{ }^\circ\text{C}$  by a ThermoFisher Accel 500 chiller, and the detectors cool by 2 K for each 3 K decrease in water temperature, so it is feasible to lower the dark current to about  $0.2\text{ e}^-/\text{pix}/\text{sec}$  when required.

Detector flatness is a concern in our fast, f/2 beam. Scans of the surfaces of Acam1 (HKO) and Acam2 (MLO) through the cryostat window when cold reveal an RMS deviation from flatness of 4 $\mu\text{m}$  for Acam1 and 9 $\mu\text{m}$  for Acam2 and a peak-to-peak deviation of 18 $\mu\text{m}$  and 36 $\mu\text{m}$ . Although Acam2 is a factor of 2 worse than Acam1, the maximum blur circle is only  $9\mu\text{m}$  (1.8") and the RMS is half of that.

These CCDs are cosmetically quite good: Acam1 has a region with bad charge transfer efficiency of about 0.2% of the area and Acam2 has a few blocked columns. The thinning leaves some artifacts but these flatten quite well; about 1% of the area is lost to the thinning border. Both of these CCDs have peculiar, low level flattening artifacts that are particularly evident in some of the horizontal sections. Acam1 has little “dipoles”, where charge from one pixel is borrowed by the one immediately below it, and Acam2 has a “bamboo forest”, where adjacent columns seem to exchange charge in a wavy pattern. It is believed that these are the result of CCD manufacturing masks with insufficient resolution, and more recent CCDs are better. These artifacts flatten quite well, so for our purposes they are not important.

Fast readout confers other problems such as bias levels that have a “plaid” pattern and must be corrected by using both serial and parallel overclocks, and cross-talk. Our  $16 \times 16$  cross-talk matrix shows values ranging between  $2 \times 10^{-4}$  to  $3 \times 10^{-5}$ , with prominent correlations between amplifiers and video boards. The cross-talk diminishes dramatically with slower clocking and we had some success in reducing it by carefully selecting pedestal and signal samples. We mark our output mask for each image with a bit indicating pixels that might be under the influence of cross-talk from some bright star, and we subtract a fraction of the image from itself according to the cross-talk matrix, but the cross-talk is not a serious issue.

Without any elastomer seals, and thanks to the ion pumps the cryostats hold vacuum very well; the cryostat on HKO was last pumped three years ago and shows no sign of leakage.

## 6. COMPUTERS AND SOFTWARE

Because we want our system to be able to run autonomously even when there is no internet connection to the observatory, we maintain a rack of computers on each summit. This rack is in a “computer room” (in fact just a reasonably dry and safe place separate from the dome), and carries an ethernet switch and six 1U “Supermicro” server computers. One is dedicated to be our gateway, one is an “admin” computer that is devoted to running the camera, and four are general purpose compute nodes. These computers each have about 12 TB of RAID1 disk, 12-16 cores (24-32 threads), and 128 GB of memory, so they are very capable and each can save approximately a month’s worth of observation. They provide substantial redundancy in case of failure.

A normal night of observation produces approximately 900 images from each of the main cameras, the auxiliary 35mm cameras, and the fisheye 35mm cameras, for a total of about 150 GB of raw, compressed data per night.

Given the good bandwidth to the observatories, our minimum latency strategy has been to perform the first reduction steps of computation at the observatory and the image subtraction and science processing at our “base cluster”. This strategy doubles the volume of data that needs to be stored at the observatory and copied, but it allows us to operate when bandwidth is poor or non-existent, and it avoids a future bottleneck if ATLAS units were to proliferate. We have a hard requirement of a latency of less than an hour from shutter close to final results, because that is the interval between the first and last observations of each field on a given night (we observe 4 or 5 times at each position across a 1 hour period). If bandwidth becomes an issue it is simple to carry out all the reductions at the observatory and copy only the final detection tables in real time, using the daylight hours to copy the images.

Our “base cluster” in Honolulu currently consists of 16 of these 1U Supermicro compute nodes and 5 4U storage computers. The storage computers carry 24 disks apiece with hardware RAID6 and each provides 120 TB (160 TB with more modern 8 GB disks) of storage. A 1U node costs about \$3,500, and a 4U storage computer costs about \$12,000. This is far less expensive than cloud storage and computation, and although we foresee eventually moving our data and processing to the cloud, it is not cost effective to do it at present.

We have adopted a philosophy of “less is better” as regards scripting languages, so we avoid high-level languages such as Perl, Python, Java, or other variants with complex dependencies so that we may provide a simplified computing environment. We have instead restricted our diversity of languages to C, bash and the usual Unix tools, and Google’s go language<sup>2</sup> for the telescope control system. This creates a significant benefit in terms of stability, computation efficiency, and most critically comprehensibility between the various software developers and users. By judicious creation of “Unix tools”, meaning programs that are designed to be used like any other Unix utility and have a man page, we have not only managed to get efficient code written efficiently, we have also created a system that is more portable, agile, and less complex than the usual GUI-oriented, scripting language rat’s nest.

Our software systems are described in detail elsewhere (Denneau et al. *in prep.*), but broadly speaking the components are:

- A telescope control system (TCS) deployed as a collection of lightweight executables written go that share system state through a Redis database.
- A scheduler that creates the desired pointings for each night and executes them.
- A reduction pipeline that is responsible for converting raw camera files into flattened, calibrated images.
- An image subtraction pipeline that matches all-sky reference images (“wallpaper”) to each image, subtracts it, and finds all the remaining sources. This employs a modified version of `hotpants` for image subtraction (Becker 2015).
- “Science clients”, specialized pieces of software that receive final images or tables and perform object selection and scientific analysis.

<sup>2</sup> <https://golang.org/>

- A post-processing pipeline that executes tasks that are important but not time critical e.g. final photometry of all stars in a reduced image.

Our primary science client is an adapted version of the Pan-STARRS Moving Object Pipeline System (MOPS; [Denneau et al. \(2013\)](#)), that links detections from different images into a plausible moving object and reports observations to the IAU Minor Planet Center (MPC). Typical execution times for a 10k observation to be processed from telescope pointing to MPC reporting are shown in Table 3. The photometry and detection programs `dophot` ([Schechter et al. 1993](#); [Alonso-García et al. 2012](#)) and `tphot`, (described in a future paper, performance reported by [Sonnott et al. \(2013\)](#)) are multithreaded, so the elapsed time is less than the CPU time. The total processing time from the moment the telescope settles on tracking the field center and the shutter opens to having an object catalog with calibrated photometry and astrometry is approximately 40 minutes of CPU time and 25 minutes of real time. The code could be optimized for somewhat better performance, but right now we are focused on higher priority development such as better science processing, better scheduling, and documentation. The deep photometry of all stars in the reduced image is an example of post-processing that is not required for our time critical science client, and this runs on some of the redundant summit computers.

A second science client is the ATLAS Transient Server that runs on a computer cluster at Queen’s University and links individual stationary detections into objects and reports supernova candidates to the IAU Transient Name Server (Smith et al, in prep.). It runs after the final detection table is created and uses the same input files as the moving object pipeline.

## 7. SYSTEM FEATURES

We have implemented a number of features to support autonomous operations and to ensure high quality data. For meteorological information we have a small “metfish” that consists of a Boltwood CloudSensor system, a Garmin GPS, and a Canon 10mm f/4 fisheye lens on a Canon 5DIII body. This “metfish” is a watertight box that uses an AR-coated glass dome intended for underwater diving to protect the lens. The Boltwood system reports temperature, wind speed, humidity, rain, and uses a thermal IR pixel to examine the sky for clouds on a 1 second cadence. The fisheye camera in our “metfish” is similar to commercial cameras<sup>3</sup>, but with additional functionality and software. A “metfish” costs about \$10,000. We use the GPS to synchronize a Stratum 1 time server, and Network Time Protocol (NTP) brings the rest of our computers to absolute time with an accuracy of a few microseconds, regardless of network connectivity to the external world.

We use the geosynchronous satellite Galaxy-15 to calibrate our shutter latency. Because Galaxy-15 is part of the GPS constellation, its position is tracked at the centimeter level by JPL and published by the National Satellite Test Bed web site<sup>4</sup>. We find that the time between initiation of a shutter movement command and when the shutter blade is half way across the aperture is  $0.281 \pm 0.017$  sec (this uncertainty arises for each Galaxy-15 observation; the repeatability suggests that the average delay is known better). Obviously our absolute exposure accuracy is limited to a few milliseconds, regardless of computer clocks that are accurate to the nearest microsecond.

The fisheye camera takes images every 5 minutes during the day, but at night switches to 32 second exposures on a 40 second cadence. The fisheye cameras at HKO and MLO are staggered by 20

<sup>3</sup> <http://www.alcor-system.com/new/index.html>

<sup>4</sup> [http://www.nstb.tc.faa.gov/rt\\_waassatellitestatus.htm](http://www.nstb.tc.faa.gov/rt_waassatellitestatus.htm)

**Table 3.** ATLAS Processing time

CPU	Elapsed	Stage
40	40	take exposure, save to disk as a raw image
40	80	flatten image
500	250	measure the brightest $\sim 60,000$ stars (dophot)
20	270	find initial astrometric solution (Lang et al. 2010)
10	280	determine final astrometric and photometric solution
20	300	perform cloud detection and correction
10	310	calculate auxiliary metadata, compress and save image
.....	.....	.....
250	560	produce wallpaper template matching image
600	1160	subtract wallpaper from image (hotpants)
750	1410	detect sources in difference image to $3\sigma$ , trim to $5\sigma$ (tphot)
180	1590	classify sources, write final detection table
120	1710	run primary science client MOPS to detect moving objects
900	610	measure $\sim 10^5$ to $\sim 2 \times 10^6$ stars (depending on galactic latitude) to $5\sigma$ (dophot)

NOTE—The typical CPU processing time (sec), cumulative elapsed wall clock time (sec), and processing stage for each 10k image are listed. Stages above the dotted line occur on the summit computers and steps below are run at the “base cluster” in Honolulu. Below the solid line are the “post-processing” stages that are run separately so as not to increase the latency of primary difference detections.

seconds so that one shutter is always open in Hawaii at night. These images are treated as scientific data and subjected to the same rigorous flattening, astrometric, and photometric calibration. We achieve astrometric residuals of about 0.1 pixel, primarily limited by the undersampled PSF and co-adding the color pixels into monochrome super-pixels, and we can achieve photometric accuracy of 0.02 mag for suitably bright stars.

The  $5\sigma$  limiting magnitude for a single fisheye image is about  $m = 7$  (depending on declination and the degree of trailing), but we have found that the sensitivity improves as  $N^{1/2}$  for  $N$  much larger than 1000. Thus a source which has average magnitude over 40 seconds of  $m = 7$  is detectable, likewise  $m = 9.5$  over an hour or  $m = 12$  over an entire night. The fisheye pixels are about 4.3 arcmin, so very faint sources are confused in stacked images, but image subtraction is very effective at removing the non-varying background.

Each fisheye image provides us with extinction measurements for up to 10,000 stars and it is easy to quantify where clouds are, how opaque they are, and how they are moving. We intend to develop a scheduler that is responsive to this information. Figure 4 illustrates the utility of the fisheye on a



night when partial clouds interrupted otherwise clear sky. The fisheye images are visible from our public website<sup>5</sup>.

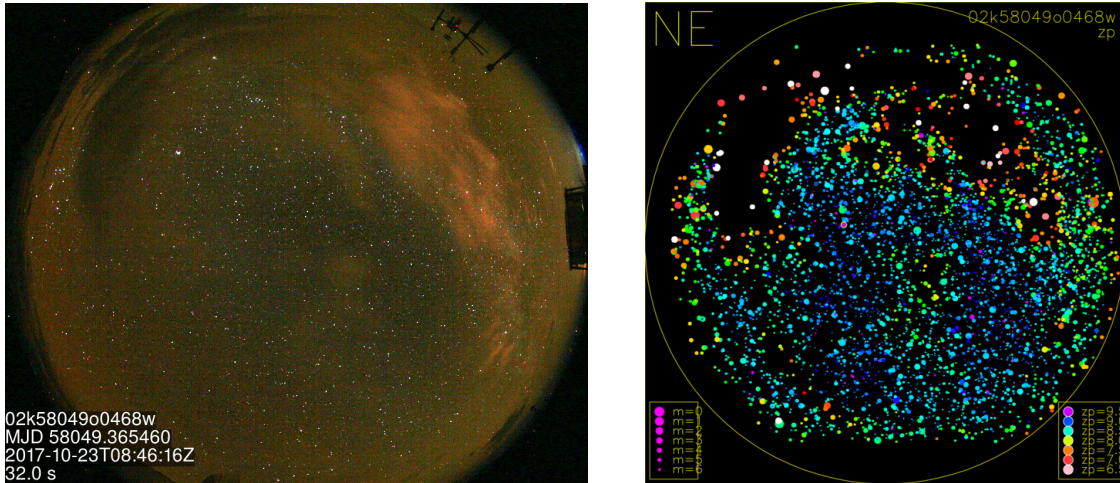


**Figure 4.** The left image shows a fisheye view of a typical partially cloudy night. Clouds are evident, but their visibility depends on the illumination (sodium light from Honolulu) and their opacity is impossible to quantify. The right image shows the zero point derived for 5,027 stars in the field, with transparency indicated by point color. The clouds are obvious, and it is also possible to quantify the effects of faint clouds and extinction.

Each dome is equipped with a Hydreon rain sensor, and each dome is powered by a small 1350 VA UPS that has enough power to close the shutter on a power failure. A Raspberry-pi monitors the Hydreon and the AC power and closes the dome when necessary regardless of what the rest of the system is doing.

Finally, we mount a Canon 5DIII and Canon 135mm f/2 lens on the telescope and take images synchronized with the main science camera. The field of view is  $15^\circ \times 10^\circ$ , easily encompassing our main field of view, and the  $5\sigma$  limiting magnitude is about  $m \sim 14$  in a 25 sec exposure. These data are processed exactly like any other, and therefore the combination of the three optical instruments allows us to monitor the sky over  $0 < m < 20$ . A summary of the ATLAS camera system is in Table 4.

## 8. PERFORMANCE RESULTS

Excluding the borders of the CCDs, our net field of view on the ATLAS Acam cameras is  $5.375^\circ$  square for a total of  $28.9 \text{ deg}^2$ , and the 900 exposures taken during a night cover  $26,000 \text{ deg}^2$ . The declination range  $-45^\circ < \delta < +90^\circ$  encompasses 85% of the sky ( $35,065 \text{ deg}^2$ ) and 25% of the sky lies within  $60^\circ$  of the Sun, which is essentially unobservable. This leaves about  $24,500 \text{ deg}^2$  of sky accessible on a given night. A single ATLAS unit could therefore cover the entire accessible sky in one night with a single 30 second exposure at each pointing.

Our mission for NASA requires us to distinguish moving objects from stationary transients, to provide a meaningful trajectory for moving objects, and to have minimal false alarms. We therefore

<sup>5</sup> <http://www.fallingstar.com>

**Table 4.** Summary of the ATLAS system cameras

Camera	Format (pixels)	Pixel size ( $\mu\text{m}$ )	Pixel Scale (arcsec)	FOV (degrees)	Dynamic range (sat. to $5\sigma$ )	Exp. Time (sec)
Acam	10560 $\times$ 10560	9	1.86	5.375 $\times$ 5.375	11–19.5	30
Canon 135mm f/2	2880 $\times$ 1920	12.6	19.4	15.5 $\times$ 10.3	4–14	25
Canon 10mm f/4 fisheye	2475 $\times$ 1920	12.6	255	180 $\times$ 150	0–7	32

NOTE—The exposure time column refers to the typical exposure time during survey operations. The 35mm camera’s pixel size refers to summed RGGB Bayer sub-pixels, the color information is kept in raw frames but not otherwise processed.

observe each field four times in a given night and reduce our Dec coverage for each unit so as to cover 1/4 of the visible sky. With two ATLAS units, our four exposure coverage is 1/2 of the visible sky each night. We therefore cover the entire accessible sky with a cadence of 2 days, with four exposures (over a 1 hour interval) reaching  $o \sim 19.5$  in each individual frames when the sky is dark and seeing good. For stationary transients the co-adds of a night’s exposures reaches  $o \sim 20.2$ .

Figure 5 shows the ATLAS sky coverage during a recent set of four nights.

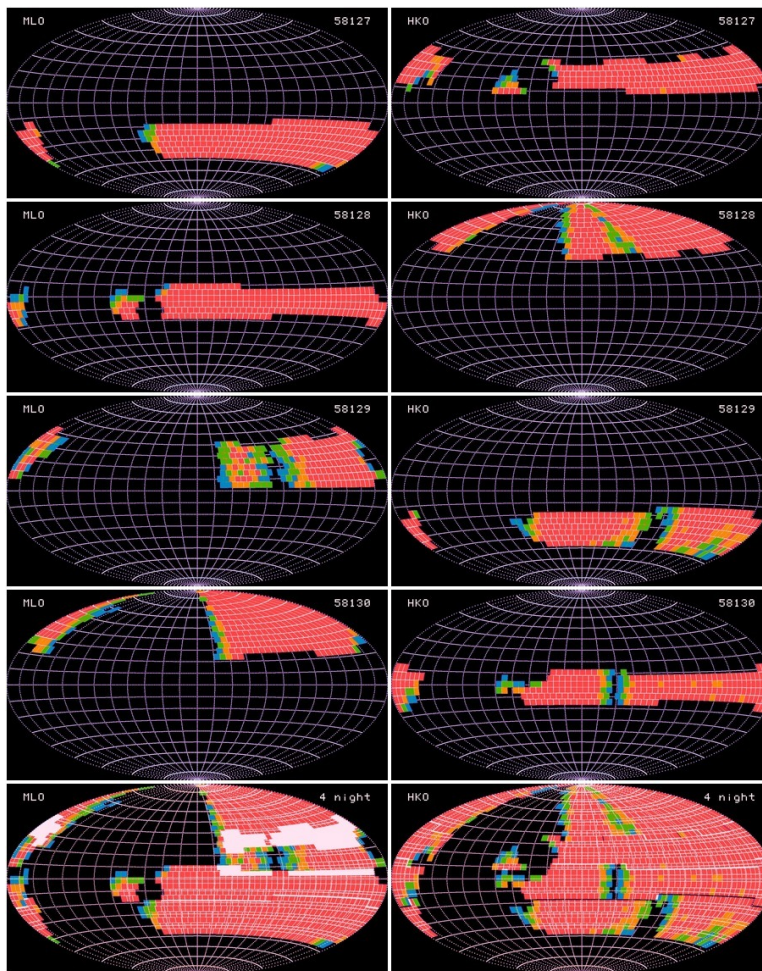


**Figure 5.** Recent ATLAS coverage of the sky over four successive nights by Mauna Loa (left) and Haleakala (right). The bottom row shows the cumulative coverage for each summit. Color codes the number of visits: blue through red is 1–4 visits. Gaps arise because of imperfect weather, duplicates because of morning clouds in the east compelled the schedule to widen Dec coverage.

There were many motivations to site both of the first two ATLAS units in Hawaii on Haleakala and Mauna Loa, one of which is weather diversity. Over the 122 days of Jun–Sep 2017, there were only 10 nights when both summits produced fewer than 450 successfully differenced images, i.e. 92% of nights were at least half workable for at least one summit. For each individual summit about 80% of nights are at least half productive, illustrating a degree of decorrelation of the weather. Similarly the fraction of nights during these 122 days for which the median zeropoint was within 0.1 mag of clear was 69% on Haleakala and 89% on Mauna Loa, and 92% of nights were clear on at least one summit.

We normally observe in  $c$  band during dark time on Haleakala and  $o$  band during bright time, and we have always observed in  $o$  band on Mauna Loa but will soon start using  $t$ . This provides color information for all the asteroids in the sky as well as other transients and variables, without compromising our sensitivity to find asteroids. Currently Haleakala can achieve a 1.9 pixel FWHM in  $o$  band and has a median of about 2.1 pixels. This degrades to 2.4 and 2.5 pixels in  $c$  band,

presumably from chromatic aberration, but the darker sky compensates and the zeropoint is about the same. The best  $5\sigma$  limiting magnitude we achieve in a 30 second exposure is 19.8 (a zeropoint of 19.5 is common), and the median over all lunations and sky conditions is 19.12. On Mauna Loa the sensitivity is just about 0.3 magnitudes worse because of the degraded PSF, and we can achieve 19.4, we often achieve 19.2, and the median is 18.83.

The FWHM and limiting magnitude performance over a recent, representative 4 month period (Jun-Sep 2017) are shown in Figure 6. It is an important priority for us to understand and improve the PSF in order to realize the full potential of our system: we are making progress but work remains. To disentangle seeing effects from defocus or mount shake we have installed a 125 mm, f/20 refractor on MLO and we have started collecting observations simultaneous with every science exposure.

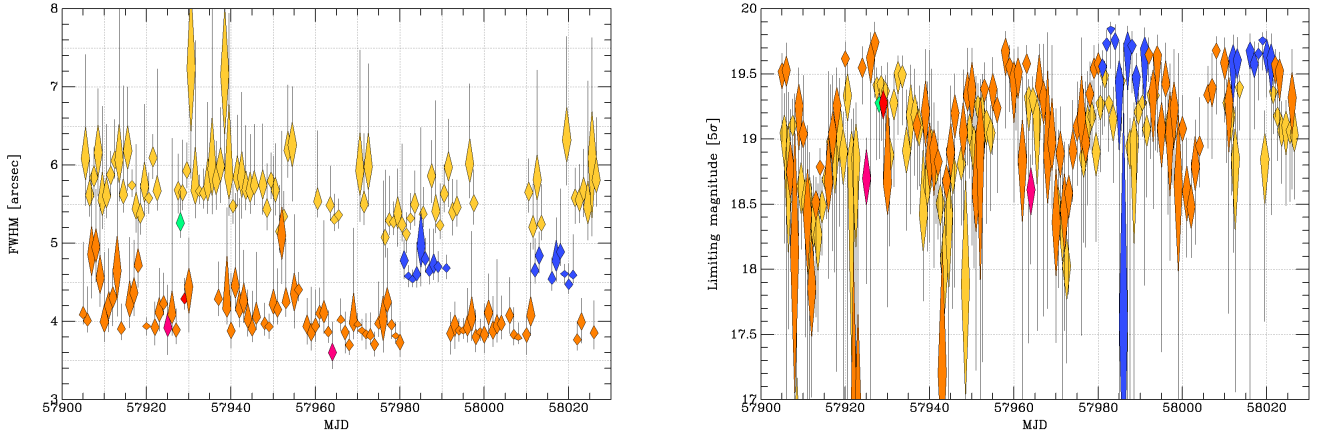


**Figure 6.** The left image shows the FWHM as a function of time and the right shows the limiting magnitude. The diamond symbols show the median and quartiles for each night, with lines extending to the 5% extremes of the distributions. The filter and site determine the point color: yellow is MLO in  $o$  band, orange is HKO in  $o$  band, blue is  $c$  band, green is  $g$ , red is  $r$ , and magenta  $i$ . The  $gri$  exposures from HKO are part of an ongoing effort to improve our photometric catalog south of  $-30^\circ$  Dec. The “limiting magnitude” is defined by where dophot reports a median uncertainty of 0.2 mag; the effect of sky brightness during four lunations is evident as well as cloudy nights.

Figure 7 shows the number of times each spot on the sky has been observed by ATLAS to date. These include both  $c$  and  $o$  filters, but only observations that are photometrically calibratable. By tying to Pan-STARRS1 reference stars (Magnier et al. 2016) most observations north of Dec  $-30^\circ$  should have photometric errors at the 0.01 mag level or lower. South of Dec  $-30^\circ$ , APASS (Henden et al. 2012) photometry is good to about 0.05 mag in systematics. We are in the process of gathering our own photometry to fill in  $g$ ,  $r$ , and  $i$  reference stars down to Dec  $-50^\circ$ . Using Gaia astrometry, there should be negligible systematic error in the positions, and the median RMS astrometric error for stars brighter than  $m = 17$  is about 70 milliarcsec; for fainter objects the error increases inversely as SNR. The release of SkyMapper’s First Data Release Wolf et al. (2018) provides another source of calibration for us to use below Dec  $-30^\circ$ , and we will soon build a new reference catalog incorporating Gaia DR2, Pan-STARRS, APASS, SkyMapper, and ATLAS photometry.

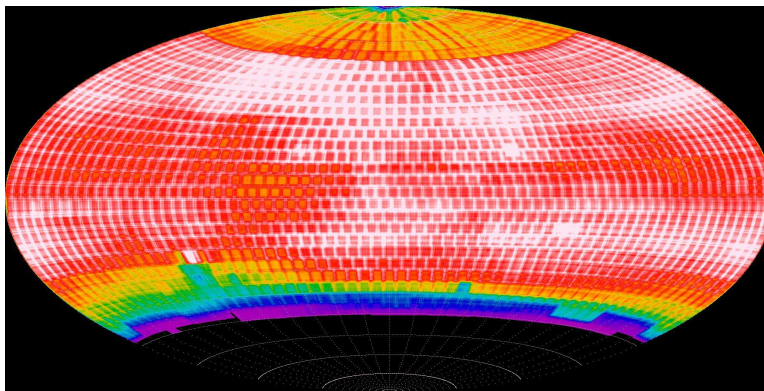


**Figure 7.** Approximately 600,000 photometrically calibrated ATLAS exposures taken between Sep 2015 and Jan 2018 are shown as a function of equatorial coordinates (left to right is RA  $360^{\circ}$ – $0^{\circ}$ ); the number of visits coded by color: cyan is 100, yellow is 300, red is 500, and white is more than 600. There 240 million stars with at least 100 light curve points from this coverage.

As of the end of January 2018 ATLAS has discovered 125 NEAs, 16 PHAs, and (somewhat surprisingly) 9 comets, and we have submitted 5.5 million observations of 128,000 distinct asteroids to the MPC. This capability is a direct result of efforts to improve sensitivity and characterization for trailed asteroids on the ATLAS detectors. ATLAS participated in the October 2017 flyby exercise of asteroid 2012 TC<sub>4</sub> and was able to detect TC<sub>4</sub> during routine operations three days before its close approach, despite the asteroid being very close to the waning full moon. ATLAS observations were submitted normally, posted on the MPC confirmation page, and even flagged as “very close” by JPL Scout hazard assessment service<sup>6</sup> before it was confirmed to be TC<sub>4</sub>.

One of the more important features of ATLAS for the overall NASA NEOO program is the ability to find very nearby objects, follow them, and report them quickly. Figure 8 shows the “candle flame” volume accessible to ATLAS for an asteroid of diameter 30 m. The probability of entering this volume is 80,000 times greater than the probability of striking the Earth. Depending on whether the near Earth population is normalized by Earth impact rates estimated by Brown et al. (2002) or Brown et al. (2013), the expectation for the number of asteroids in this volume at any given instant is either 2 or 9, and the refresh rate is approximately 5 days. Given full sensitivity to streaked detections and allowing for moon and clouds, ATLAS should be able to see about 10–50 NEAs of size 30 m per year, depending on which of these normalizations is correct.

NEA detection and discovery statistics shown in Figure 9 illustrate ATLAS’ successful optimization for its mission of detecting asteroids passing near the Earth. While other surveys with larger telescopes and greater sensitivity discover many more asteroids per year, ATLAS’ very rapid sky coverage gives it a unique ability to detect almost all the asteroids that brighten past its sensitivity limit in any given interval of time. During the period covered by Figure 9 (June–September 2017), ATLAS detected 75% of all NEAs determined by after-the-fact ephemerides to have brightened past magnitude 19.0 at declination north of  $-35^{\circ}$  and solar elongation greater than  $90^{\circ}$ . The 287 NEAs used to calculate this statistic include challenging objects that remained above the 19th magnitude detection threshold for less than one day; became observable only near full Moon; or were moving as

<sup>6</sup> <https://cneos.jpl.nasa.gov/scout/>

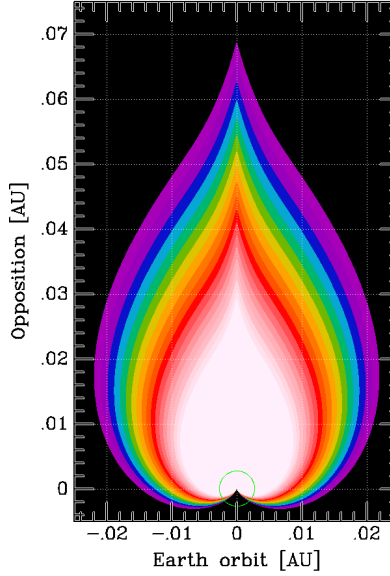


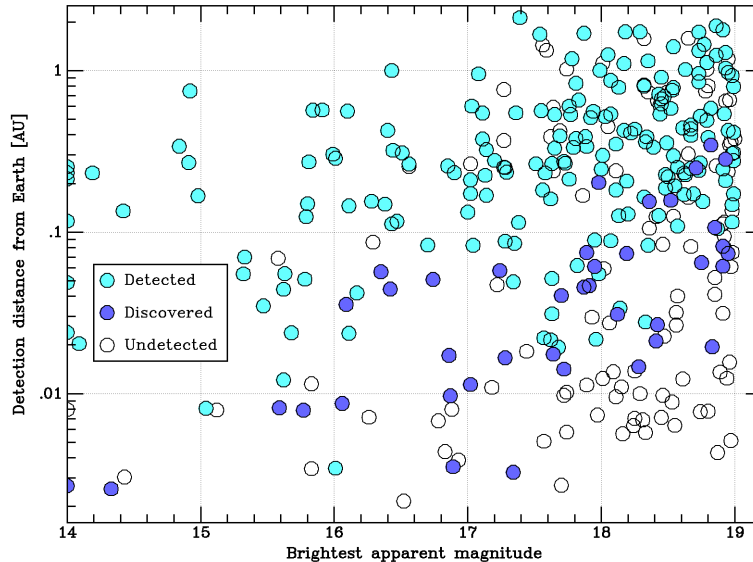
**Figure 8.** The volume in which a 30 m diameter asteroid with typical phase function and albedo would be visible to ATLAS is shown with color coding the probability that the asteroid would be seen: black is 0.0, yellow is 0.5, and white is 1.0. The Moon’s orbit is a green circle, and the Sun is at  $(0, -1)$  AU. A typical asteroid will cross 0.01 AU in a day. The probabilities are derived from the actual performance of Haleakala during a recent, representative four month span; moon and clouds cause the variation in probability and volume.

fast as 50 deg/day at the moment of their closest approach. Of the 75% of sufficiently bright NEAs that were detected by ATLAS, 19% (40 NEAs) were ATLAS discoveries, and most of these would not even be known to exist or to have passed Earth apart from ATLAS. The 25% of potentially detectable NEAs that ATLAS missed includes some that were discovered earlier and not recovered by any survey during their 2017 apparition. Thus, within a generous range of parameters that includes very difficult cases, NEAs passing Earth had only a 25% chance of escaping ATLAS’ net in late 2017.

This 25% statistic does not, of course, include an unknown number of NEAs that passed by Earth without being discovered by *any* survey. The total number of small yet dangerous NEAs that inhabit the Solar System is still uncertain to within a factor of a few – but ATLAS is poised to measure it much more accurately over the coming years.

In this context, we can consider ATLAS’ ability to detect asteroids in the size range of the object that likely produced the Tunguska explosion in 1908, which devastated more than 2000 km<sup>2</sup> of Siberian forest. This object likely had an absolute magnitude of  $H \sim 25$ , which corresponds to a diameter of 60m for a 5% albedo. We like to use the term ‘Tunguska-level near miss’ to describe cases when asteroids at least this large are discovered during Earth encounters that bring them closer than 0.01 AU. Neglecting gravitational focusing, there should be one actual Tunguska-like impact for every 55,000 Tunguska-level near misses. During the June-September 2017 period covered by Figure 9, there were seven known Tunguska-level near misses, which may be naively translated into an impact rate of one per 3000 years. Of the seven near-misses, ATLAS discovered three and Catalina and Pan-STARRS each discovered two. Thus, although the larger telescopes of the other surveys enable them to discover far more NEAs than ATLAS overall (including larger, globally hazardous

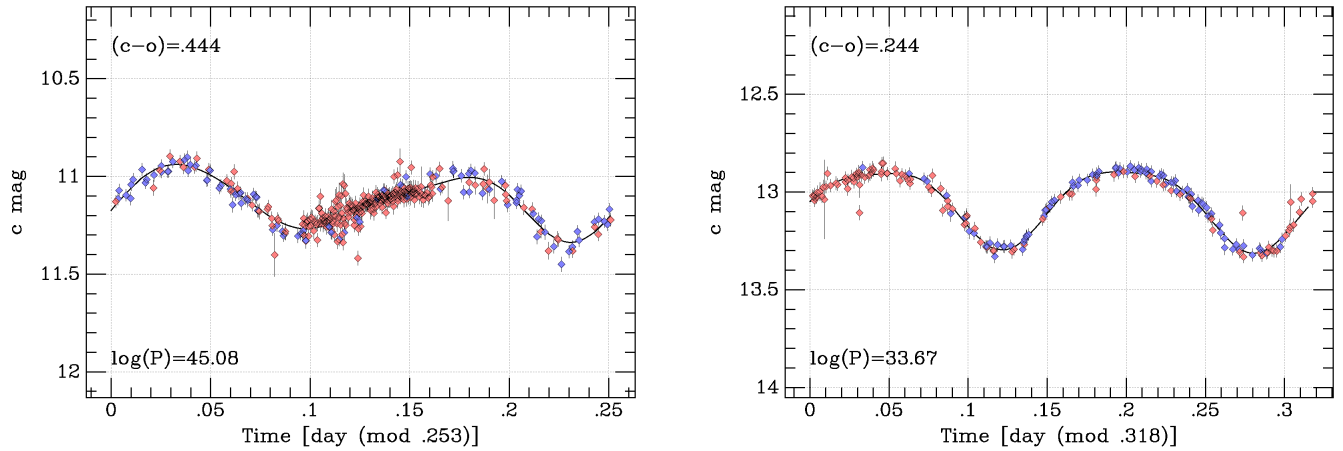
asteroids passing Earth at larger distances), in the specific case of regionally dangerous asteroids passing very close to the Earth, ATLAS is competitive with far more expensive surveys. We note also that six out of the seven Tunguska-level near misses were detected by only one of the major surveys. This lack of overlap suggests that only a minority of the actual Tunguska-level near misses are detected by any survey – a gap in our current planetary defence that can be most efficiently filled by building more ATLAS units. When the NEA population statistics are finally determined, the rate of Tunguska-like impacts will likely turn out to be considerably higher than the naive estimate quoted above.



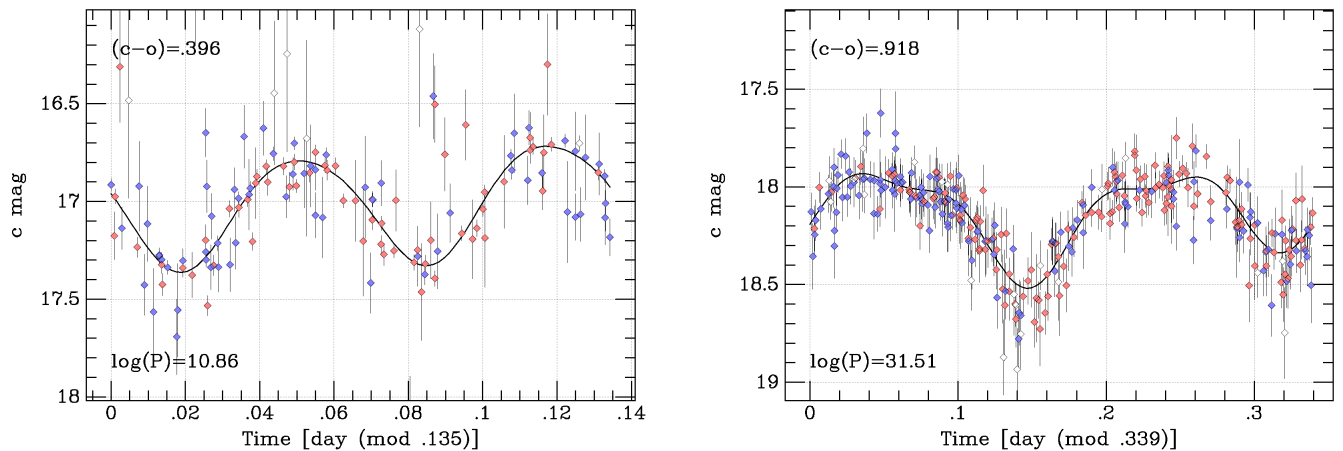
**Figure 9.** ATLAS detected NEAs as a function of Earth distance over the 122-day interval 01 June 2017 through 30 September 2017. The magnitude either refers to ATLAS  $c$  or  $o$  for ATLAS detections or else  $V$  band. The white points are NEAs that were either previously known or discovered by another survey first during this period, but not detected by ATLAS. Cyan and blue points are NEAs that were detected by ATLAS, with blue indicating that ATLAS was the discoverer. ATLAS is very efficient at detecting nearby asteroids that are brighter than  $m < 19$ , and is particularly effective for discovering NEAs closer than 0.1 AU.

Figure 10 shows lightcurves for a typical bright asteroid and a typical bright variable star. Figure 11 shows lightcurves for an asteroid that is 15 times smaller and a variable star that is 100 times fainter. ATLAS has analyzed 2 year lightcurves with at least 100 points for about 20,000 asteroids and 140 million stars between  $-30^\circ < \delta < +60^\circ$  and  $m < 18$ , and detected 5 million stars which show variability (Heinze et al. *in prep.*). These lightcurves will be available from MAST at Space Telescope Science Institute. Observation to date has increased the number of stars to 240 million between  $-45^\circ < \delta < +90^\circ$ .

Our improved photometry enables light curve science with ATLAS data. We have observations of  $\sim 300,000$  numbered asteroids, and as of 2017 (prior to replacement Schmidt correctors) we were able to assign a period to 20,000 of them using standard period searches followed by deep machine learning using the R programming language to classify the candidate lightcurves. This dataset alone is as large as the current published asteroid lightcurve database and includes thousands of previously



**Figure 10.** The left image shows the H magnitude phased light curve for the bright asteroid 700, and the right image a bright, AAVSO eclipsing binary star. Point color indicates  $c$  (blue) or  $o$  (orange) filters; the  $o$  magnitudes are shifted by the listed  $(c - o)$  color. “ $\log(P)$ ” is  $-\log$  of the false alarm probability reported by Lomb-Scargle. The ATLAS sampling and coverage can recover an accurate period as well as color, even though the observations span many periods. ATLAS has lightcurves for 240 million other stars and asteroids.



**Figure 11.** The left image shows the H magnitude phased light curve for the near Earth asteroid 1997 XF11 (35396) that rotates every 3.26 hours, and the right image an uncataloged eclipsing binary star with a period of 8.15 hours. White points are deemed outliers and not included by our Lomb-Scargle program.

unknown asteroid lightcurves. Continued ATLAS observations will only improve the number and quality of asteroid lightcurves in the ATLAS dataset.

ATLAS has been a partner in LIGO - Virgo Consortium searching for optical counterparts for gravitational wave events (Abbott et al. 2016, 2017c; Stalder et al. 2017) The ATLAS survey is particularly well-suited because our system covers such a large sky area that we do *not* require targeted scheduling to cover areas of interest when LIGO events occur. We can provide the history of variability or transient activity in LIGO-Virgo skymap to reduce the astrophysical false positives and



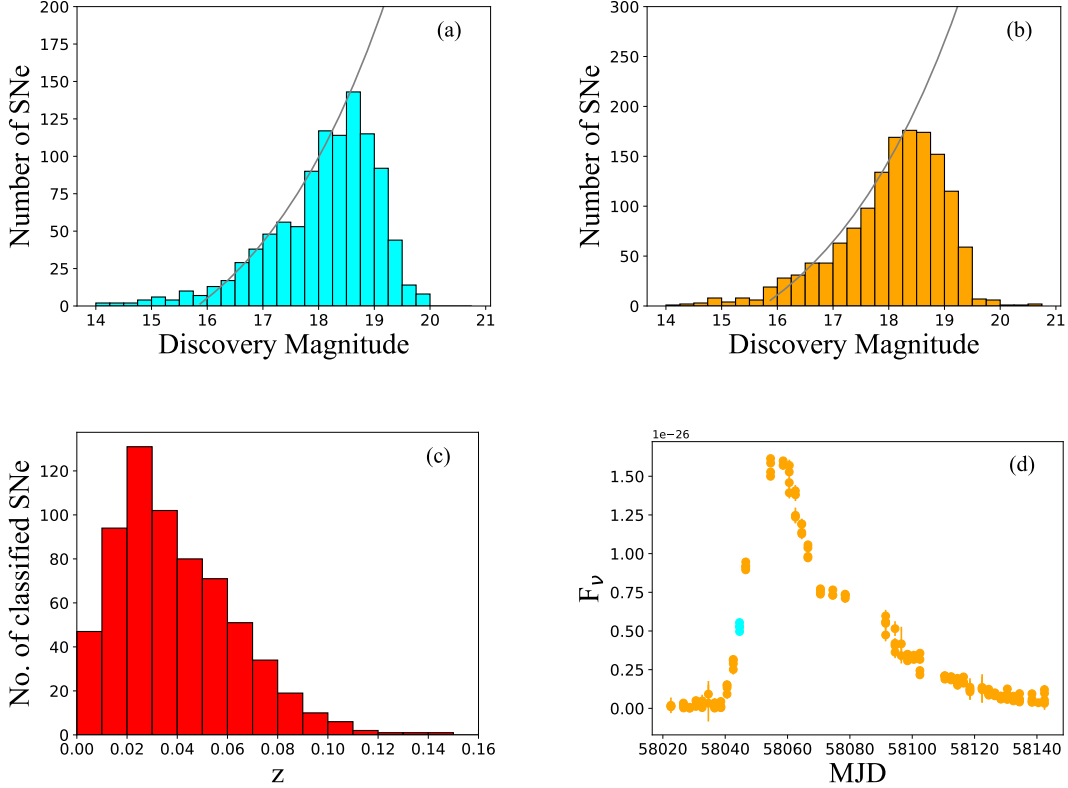


**Figure 12.** (a): histogram of discovery magnitudes of the 1075 ATLAS detected SNe in the cyan filter. This includes our own discoveries, and those discovered by other surveys, but which are independently detected in our survey. (b): histogram of discovery magnitudes of the 1441 ATLAS detected SNe in the orange filter. (c): histogram of redshifts of the 654 classified SNe (only a small fraction of discoveries receive the followup required for secure classification). (d): forced photometry (flux vs epoch) of SN2017hjl at  $z = 0.016$ , obtained from the normal observations seeking asteroids.

reject associations. The one electromagnetic counterpart discovered so far, AT2017gfo (associated with GW170817), was remarkably bright when discovered at 0.47 days after the GW trigger. From the early *gri* photometry of Arcavi et al. (2017b); Drout et al. (2017); Coulter et al. (2017), we estimate its peak brightness within the first day was  $c \sim 17.4$  and  $o \sim 17.3$ , comfortably above the routine ATLAS survey limits. We were unfortunate with the sky placing, since we had stopped observing that RA range just 16 days before. Up to that point ATLAS had 601 individual images of NGC4993, providing a simple but important statement that no variable or transient object had ever been detected at that position and provided a temporal constraint for the 4-dimensional probability (3 space and one of time) of coincidence of the optical transient and the gravitational wave (as discussed in Smartt et al. 2017). With our large sky area coverage, 2 day cadence and rapid data processing ATLAS will play an important role in the detection of future electromagnetic counterparts in LIGO-Virgo’s O3 run beginning 2018, and will also provide an independent search for kilonova without a GW trigger, within a volume of about 60 Mpc.

Figure 12 shows the earliest ATLAS magnitudes of all 2476 candidate extragalactic transients we have identified since 21 Dec 2015, the overwhelming majority of which are supernovae. In this figure

we do not distinguish between those supernovae that were discovered (i.e. first report to the TNS) by other surveys and those that were exclusively discovered first by ATLAS. The reason for doing this is to highlight the ATLAS detection performance, rather than speed and competitiveness of reporting. At  $m = 19 \pm 0.2$  we are roughly 50% complete assuming that supernovae are isotropically distributed in the local volume. We also show an example of the lightcurve of an ATLAS supernova (ATLAS17mgh, recorded as SN2017hjj on the TNS, also seen by Gaia as Gaia17crm) with forced photometry (flux vs epoch). This is a type Ia in UGC03245 at  $z = 0.016$  and a spectrum was taken about 1 week before maximum light by the Asiago Transient Classification Program (Tomasella et al. 2014; Tomasella et al. 2017), enabled by the immediate, public discovery announcement by ATLAS. The secondary peak in the lightcurve is nicely visible in the  $o$ -band filter. We also show the redshift distribution of the 654 spectroscopically classified supernovae in Figure 12. A full description of the ATLAS transient pipeline and early science results will be discussed in Smith et al. (in prep).

## 9. CONCLUSIONS

ATLAS represents another step in the relentless march toward increased time-domain coverage of the sky. With ATLAS, the complete northern sky is now observed every two days to fainter than  $m = 19$ . The system routinely and automatically executes its mission of surveying for dangerous NEAs. The low cost and reproducibility of an ATLAS unit means that the system capability is relatively easy to extend.

ATLAS stands on the shoulders of many other broad advances—Gaia for exquisite astrometry, Pan-STARRS for photometric calibration and its MOPS pipeline, `astrometry.net` for blind astrometric reduction, to name several—all facilitated by inexpensive, high-performance computers. Although we are not outfitted to serve ATLAS data products to the community, ATLAS data are available to any institution able to receive our data, with no proprietary period.

Prospects for extending the ATLAS system to cover the remaining southern sky are excellent – there are plans awaiting funding to construct two ATLAS units in the southern hemisphere longitudinally opposite Hawai‘i. These additional units will allow the entire system to re-observe the entire sky every 24 hours (and every 12 hours for some of the sky). The weather diversity and continuous sky coverage of such a configuration will improve the ATLAS dataset in areas where it already excels:

- Tightening the net for NEA discovery. While the current collection of all-sky NEA surveys (Pan-STARRS 1, Catalina Sky Survey and ATLAS) continue to increase their discovery rates, many detectable NEAs still go undiscovered each lunation. A full-sky, nightly ATLAS system will reduce the number of undetected NEAs that sneak by the Earth, and the well-calibrated and characterized ATLAS system will help quantify global NEA survey effectiveness.
- Denser coverage for transients. Detectable supernovae will be observed within 12-24 hours of explosion, increasing the likelihood of seeing shock breakout and obtaining followup spectra during the very interesting early stages of the explosion.
- New variable stars in challenging classes. These include stars with very small amplitudes; variables currently difficult to measure due to frequency aliasing such as RR Lyrae stars and contact binaries with periods near 0.5 or 1.0 sidereal days; and extremely long-period Mira stars and other pulsating supergiants.

- Immediate followup of any LIGO/Virgo transients. The flexible asteroid survey can rearrange its target list such that an ATLAS telescope can be pointed at a candidate LIGO/Virgo event within 60 seconds.

## 10. ACKNOWLEDGEMENTS

We acknowledge useful discussions with Gaspar Bakos, Klaus Hodapp, Robert Jedicke, Eileen Ryan, Tim Spahr and Richard Wainscoat. Support for this work was provided by NASA grant NN12AR55G under the guidance of Lindley Johnson and Kelly Fast. We acknowledge support for transient science exploitation from the EU FP7/2007-2013 ERC Grant agreement n° [291222], STFC Grants ST/P000312/1, ST/N002520/1 and support from the QUB Kelvin HPC cluster, and the QUB International Engagement Fund. We thank Mike Bessell for discussions on the design of our filter set and sharing the Skymapper experience.

## REFERENCES

- Abbott, B. P., Abbott, R., Abbott, T. D., et al. 2016, *ApJL*, 826, L13
- . 2017a, *Physical Review Letters*, 118, 221101
- . 2017b, *Physical Review Letters*, 119, 161101
- . 2017c, *ApJL*, 848, L12
- Alonso-García, J., Mateo, M., Sen, B., et al. 2012, *AJ*, 143, 70
- Arcavi, I., Hosseinzadeh, G., Brown, P. J., et al. 2017a, *ApJL*, 837, L2
- Arcavi, I., Hosseinzadeh, G., Howell, D. A., et al. 2017b, *Nature*, 551, 64
- Bañados, E., Venemans, B. P., Morganson, E., et al. 2014, *AJ*, 148, 14
- Baltay, C., Rabinowitz, D., Hadjijska, E., et al. 2013, *PASP*, 125, 683
- Becker, A. 2015, HOTPANTS: High Order Transform of PSF ANd Template Subtraction, Astrophysics Source Code Library, [ascl:1504.004](https://arxiv.org/abs/1504.004)
- Bellm, E. 2014, in *The Third Hot-wiring the Transient Universe Workshop*, ed. P. R. Wozniak, M. J. Graham, A. A. Mahabal, & R. Seaman, 27
- Bellm, E. C. 2016, *PASP*, 128, 084501
- Bessell, M., Bloxham, G., Schmidt, B., et al. 2011, *PASP*, 123, 789
- Bessell, M., & Murphy, S. 2012, *PASP*, 124, 140
- Brown, P., Spalding, R. E., ReVelle, D. O., Tagliaferri, E., & Worden, S. P. 2002, *Nature*, 420, 294
- Brown, P. G., Assink, J. D., Astiz, L., et al. 2013, *Nature*, 503, 238
- Centko, S. B., Kulkarni, S. R., Horesh, A., et al. 2013, *ApJ*, 769, 130
- Centko, S. B., Urban, A. L., Perley, D. A., et al. 2015, *ApJL*, 803, L24
- Chambers, K. C., Magnier, E. A., Metcalfe, N., et al. 2016, ArXiv e-prints, [arXiv:1612.05560](https://arxiv.org/abs/1612.05560) [[astro-ph.IM](https://arxiv.org/abs/1612.05560)]
- Coulter, D. A., Foley, R. J., Kilpatrick, C. D., et al. 2017, *Science*, 358, 3
- Dark Energy Survey Collaboration, Abbott, T., Abdalla, F. B., et al. 2016, *MNRAS*, 460, 1270
- Denneau, L., Jedicke, R., Grav, T., et al. 2013, *Publications of the Astronomical Society of the Pacific*, 125, 357
- Dong, S., Shappee, B. J., Prieto, J. L., et al. 2016, *Science*, 351, 257
- Drake, A. J., Djorgovski, S. G., Mahabal, A., et al. 2009, *ApJ*, 696, 870
- Drout, M. R., Piro, A. L., Shappee, B. J., et al. 2017, *Science*, 358, 1570
- Foley, R. J., Scolnic, D., Rest, A., et al. 2018, *MNRAS*, 475, 193
- Fukugita, M., Ichikawa, T., Gunn, J. E., et al. 1996, *AJ*, 111, 1748
- Gaia Collaboration, Prusti, T., de Bruijne, J. H. J., et al. 2016, *A&A*, 595, A1
- Gal-Yam, A., Kasliwal, M. M., Arcavi, I., et al. 2011, *ApJ*, 736, 159
- Henden, A. A., Levine, S. E., Terrell, D., Smith, T. C., & Welch, D. 2012, *Journal of the American Association of Variable Star Observers (JAAVSO)*, 40, 430

- Hodgkin, S. T., Wyrzykowski, L., Blagorodnova, N., & Koposov, S. 2013, *Royal Society of London Philosophical Transactions Series A*, 371, 20239
- Holoien, T. W.-S., Stanek, K. Z., Kochanek, C. S., et al. 2017, *MNRAS*, 464, 2672
- Hsieh, H. H., Yang, B., Haghhighipour, N., et al. 2012, *ApJL*, 748, L15
- Keller, S. C., Schmidt, B. P., Bessell, M. S., et al. 2007, *PASA*, 24, 1
- Kuncarayakti, H., Maeda, K., Ashall, C. J., et al. 2017, ArXiv e-prints, [arXiv:1712.00027](https://arxiv.org/abs/1712.00027) [[astro-ph.SR](#)]
- Laevens, B. P. M., Martin, N. F., Bernard, E. J., et al. 2015, *ApJ*, 813, 44
- Lang, D., Hogg, D. W., Mierle, K., Blanton, M., & Roweis, S. 2010, *AJ*, 139, 1782
- Law, N. M., Kulkarni, S. R., Dekany, R. G., et al. 2009, *PASP*, 121, 1395
- Lipunov, V. M., Gorbovskey, E., Kornilov, V. G., et al. 2017, *ApJL*, 850, L1
- Liu, M. C., Magnier, E. A., Deacon, N. R., et al. 2013, *ApJL*, 777, L20
- Magnier, E. A., Schlafly, E. F., Finkbeiner, D. P., et al. 2016, ArXiv e-prints, [arXiv:1612.05242](https://arxiv.org/abs/1612.05242) [[astro-ph.IM](#)]
- Moriya, T. J., Tanaka, M., Yasuda, N., et al. 2018, ArXiv e-prints, [arXiv:1801.08240](https://arxiv.org/abs/1801.08240) [[astro-ph.HE](#)]
- Nicholl, M., Smartt, S. J., Jerkstrand, A., et al. 2014, *MNRAS*, 444, 2096
- . 2015, *ApJL*, 807, L18
- Quimby, R. M., Kulkarni, S. R., Kasliwal, M. M., et al. 2011, *Nature*, 474, 487
- Rest, A., Scolnic, D., Foley, R. J., et al. 2014, *ApJ*, 795, 44
- Schechter, P. L., Mateo, M., & Saha, A. 1993, *PASP*, 105, 1342
- Scolnic, D., Kessler, R., Brout, D., et al. 2018, *ApJL*, 852, L3
- Smartt, S. J., Valenti, S., Fraser, M., et al. 2015, *A&A*, 579, A40
- Smartt, S. J., Chen, T.-W., Jerkstrand, A., et al. 2017, *Nature*, 551, 75
- Soares-Santos, M., Holz, D. E., Annis, J., et al. 2017, *ApJL*, 848, L16
- Sonnett, S., Meech, K., Jedicke, R., et al. 2013, *PASP*, 125, 456
- Stalder, B., Tonry, J., Smartt, S. J., et al. 2017, *ApJ*, 850, 149
- Tanvir, N. R., Levan, A. J., González-Fernández, C., et al. 2017, *ApJL*, 848, L27
- Terebizh, V. Y. 2011, *Astronomische Nachrichten*, 332, 714
- . 2016, *AJ*, 152, 121
- Tomasella, L., Benetti, S., Cappellaro, E., et al. 2014, *Astronomische Nachrichten*, 335, 841
- Tomasella, L., Benetti, S., & Cappellaro, E. 2017, *The Astronomer's Telegram*, 10863
- Tonry, J. L. 2011, *PASP*, 123, 58
- Tonry, J. L., Stubbs, C. W., Kilic, M., et al. 2012, *ApJ*, 745, 42
- Valenti, S., David, Sand, J., et al. 2017, *ApJL*, 848, L24
- Walton, N., Hodgkin, S., & van Leeuwen, F. 2015, *IAU General Assembly*, 22, 2257872
- Wolf, C., Onken, C. A., Luvaul, L. C., et al. 2018, ArXiv e-prints, [arXiv:1801.07834](https://arxiv.org/abs/1801.07834) [[astro-ph.IM](#)]